


Dust, sand and wind drive slope streaks on Mars

Received: 18 July 2025

Accepted: 17 October 2025

Published online: 06 November 2025

 Check for updatesValentin Tertius Bickel  

Mars' slope streaks are dark albedo features created by the avalanching of surface dust. Recent work provided geostatistical evidence for the dry nature of streaks and their drivers, but presented no direct, quantitative measure of streak formation rates and seasonality. Here, I associate the global, spatio-temporal occurrence of more than 2.1 million slope streaks, identified between 2006 and 2024, with their hypothesized dry, (non)seasonal drivers: meteoroid impacts, marsquakes, and wind action. Streak formation rates vary across Mars and time, with an average of ~0.05 newly-formed streaks per existing streak per Mars Year. Only ~0.1 % of the annually formed streak population can be directly attributed to non-seasonal processes like meteoroid impacts and quakes. The bulk of streak formation coincides with the seasonal delivery of atmospheric dust and peaks in the southern summer and autumn, when wind stress systematically exceeds the threshold required for the initiation of sand saltation and dust mobilization. The conditions most conducive to seasonal streak formation appear to occur at sunrise and sunset, explaining the lack of direct observations of streak forming events to date. This work underscores the dry nature of slope streaks and enumerates their potentially important role in the Martian dust cycle.

Slope streaks are dark albedo features on Martian slopes that have been associated with the transient presence of liquid water or brines since their discovery in the 1970s^{1–6}. A recent study used a global, deep learning-enabled, geostatistical approach to suggest a purely dry nature of slope streaks on Mars⁷, agreeing with the conclusions presented by preceding regional studies (e.g., refs. 8–12). Bickel and Valantinas⁷ also reported statistical evidence for the decisive role of atmospheric dust delivery and dry, energetic triggers in driving the formation of slope streaks, specifically meteoroid impacts, marsquakes, and near-surface winds and gusts. Yet, Bickel and Valantinas⁷ limited their analysis to Dickson et al.'s¹³ MRO CTX (Mars Reconnaissance Orbiter Context Camera¹⁴) global mosaic, which represents one snapshot in time, inhibiting any direct, sophisticated spatiotemporal correlation of slope streak distribution and formation with other relevant datasets, such as atmospheric models and catalogs of impact- and tectonic events.

Here, I use an improved, deep learning-driven approach to identify slope streaks in the full CTX image archive, enabling a holistic

analysis of slope streak occurrence and formation in space and time, all across Mars. I use this dataset to (1) investigate the distribution, magnitude, rate, and seasonality of slope streak formation across the planet, (2) quantify the contribution of the three main drivers of streak formation to the overall streak production, and (3) estimate the potential contribution of slope streak formation to Mars' overall atmospheric dust budget. This study represents a holistic, spatio-temporal investigation of one of Mars' most enigmatic, transient surface features, with important implications for our understanding of modern Mars' surface-to-atmosphere interactions and the dust cycle in general.

Results

Global streak formation rates and seasonality

I identify 2,169,234 individual slope streaks in 91,687 CTX images acquired between 2006 and 2024 (including MRO orbit 84,839, September 2024), covering Mars between 55°N and 35°S multiple times over. This census intentionally includes a substantial fraction of

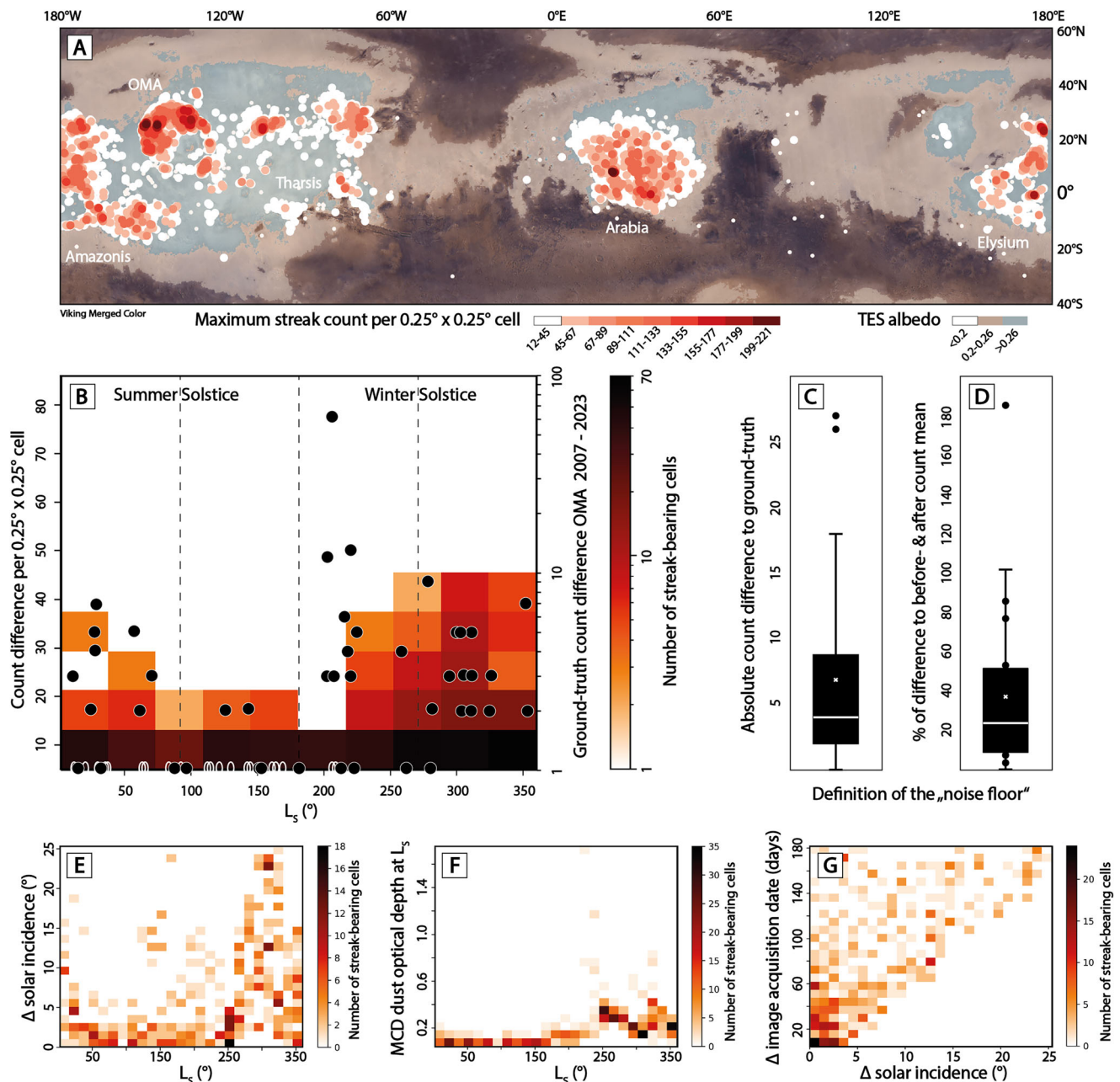


Fig. 1 | Distribution, formation rates, and seasonality of Martian slope streaks.

A map of the maximum number of streaks identified in each grid cell, considering all available CTX images, overlain on a Viking Merged Color mosaic and a transparent TES (Thermal Emission Spectrometer) albedo map (60°N to 40°S), highlighting dust-rich (0.2–0.26, tan) and very dust-rich (>0.26, blue) regions, following ref. 7. Five distinct, global streak populations are highlighted: Amazonis, OMA (Olympus Mons Aureole), Tharsis, Arabia, and Elysium. Small white dots indicate cells with counts between 12 and 15 streaks. **B** heatmap of the relation between streak count difference (left y axis) and seasonality per cell (L_s , number of cells considered is 596); manual ground-truth measurements overlain (black dots, right x axis); white ellipses indicate (manually scanned) image pairs without any change. Manual counts were derived using images acquired between 2007 and 2023. The

accuracy of the results presented in (**B**) is dependent on the noise floor of the detection method itself and is affected by the tradeoff between the allowed maximum image acquisition date delta (here, 6 months or $\sim 90^\circ L_s$) and data abundance, which reduces the temporal resolution or temporal accuracy of the detector-derived count differences; this inaccuracy is likely causing the slight temporal offset between the detector-derived and manual counts. **C** and **D** quantify the accuracy of the automated detection method using ground-truth data, as absolute counts and as a percentage, respectively. Relation of the difference of solar incidence between image pairs and season (**E**), MCD column-integrated dust optical depth and season (**F**), and the difference of solar incidence between image pairs and the time between image pair acquisitions (**G**), per considered (slope streak-bearing) cell (as used for **B**).

duplicate detections, as streaks persist over years and decades, appearing in several subsequent CTX images. All streak detections are binned into $0.25^\circ \times 0.25^\circ$ cells; the highest density of streak-bearing cells ('maximum count') is located in five globally distinct streak 'hot-spots': Amazonis, OMA (Olympus Mons Aureole), Tharsis, Arabia, and Elysium, agreeing with earlier global mapping efforts⁷ (Fig. 1A).

features the highest density and number of streak-bearing cells, with a peak maximum count of 221 streaks/cell (Fig. 1A), while Arabia features the spatially most-extensive, coherent region of slope-bearing cells. Integrating the maximum counts for all cells and adjusting them for the effect of spatially co-located (nested) streaks as well as for the recall of the used detector ($\sim 75\%$), the data suggest there are ~ 1.6

million CTX-scale slope streaks all across Mars, which is slightly lower than the ~1.9 million slope streaks estimated earlier by Bickel and Valantinas⁷, but twice as high as previous estimates by Aharonson et al.¹⁵.

Considering cells with image pairs that were acquired with a temporal difference of less than 6 months and that feature 100% spatial overlap with the respective cell, I derive differences in streak counts over time ('difference counts'). Differences in streak counts per cell over time can be indicative of streak formation and fading, but – importantly – can also be caused by variations in imaging geometry and atmospheric conditions (false changes). Most prominently, changes in the atmospheric dust load and solar incidence angle, as well as spatial shifts caused by minor image geolocation inaccuracies can lead to the detection of false changes; for example, streaks that were shadowed in the first image of a pair are illuminated in the second image, which enables their detection – and thus mimics their formation (Fig. S1). I characterize the median 'noise floor' caused by false changes using a set of 100 ground-truth cells (Fig. 1C, D) and only consider difference counts that exceed the median noise floor, to minimize the impact of false changes. Here, the term noise floor describes the threshold that is used to distinguish between valid (i.e., used for the analysis) and invalid changes (i.e., not used for the analysis), in a statistical way.

My workflow identifies substantially (globally) enhanced streak count differences – more cells with higher count differences – during the southern summer and fall, with a peak between L_S -220° and -360°, and a less pronounced tail that extends until L_S -60° (Fig. 1B). These peaks indicate distinct, seasonally enhanced streak formation rates, and agree with the results presented by earlier surveys conducted in specific regions on Mars^{12,16}. Most considered cells host low numbers of newly formed streaks (<10), but there are 'bursts' of streak formation with more than ~40 features that form between two images. As observed earlier by Bickel and Valantinas⁷, the used streak detector tends to identify spatially co-located (nested) streaks as one single feature, suggesting that the detector-derived burst counts underestimate the actual (absolute) number of individual streaks that formed by a factor of ~2, on average.

I conduct a detailed, manual ground-truth time-series spot-check of two separate OMA slope streak monitoring cells centered at 24°N, 147°W and 28°N, 145°W using 77 images acquired between 2007 and 2023. The results of the spot-check (Fig. 1B) closely agree with both the number of the detector-observed newly formed streaks as well as their seasonal timing. The spot-check also confirms the observation that streak formation can happen steadily (<10) and in bursts (>40) between consecutive images. Notably, the locations of highly active cells (derived by manual and detector counts) closely resemble the spatial distribution of cells with high to very high maximum streak counts, implying that the three independent measures of streak activity agree.

Using the first and most recent images taken of each analysis cell, I compute a global streak formation rate with the longest-possible temporal baseline (Δ_t , average of ~5.2 MY, and a minimum of 1 MY). Globally, all considered cells experience an average, normalized streak formation rate of ~5.5%/MY. This rate (5.5%/MY, for $\Delta_t > 1$ MY) and the number of slope streaks estimated to be present across Mars ($n = 1,600,000$), along with two additional rates derived from image pairs with $\Delta_t > 2$ MY (4.6%/MY) and $\Delta_t > 3$ MY time difference (4.2%/MY) suggests that between ~88,000, ~73,600, and ~67,200 CTX-scale streaks should form per MY all over Mars. This implies that Mars' entire streak population would be replenished within ~18 to ~24 MY, assuming that the overall population of streaks remains constant.

Sporadic, higher-than-average formation rates (up to ~88%/MY) can exclusively be attributed to streak bursts that happened at locations with few pre-existing streaks and between images with a relatively short temporal baseline ($\Delta_t \sim 1$ MY) and do not represent the

long-term formation rate of the majority of the streak population. Image pairs with a difference of at least 3 MY suggest that the highest long-term formation rates (up to ~28%/MY) occur across all major hotspots, with the exception of Elysium (Fig. S2). Overall, these formation rates are in line with earlier, regional estimates of streak formation (~3 to ~7.9%/MY, with peaks up to ~30%/MY^{12,15–18} as well as previous estimates of streak lifetime (~11 to ~22 MY)^{17–19}, although the increased number of streaks that were mapped across Mars⁷ leads to higher absolute formation rates of streaks than previously estimated (~factor ~1.3 to ~1.8)¹⁵, further establishing slope streaks as a highly dynamic geologic process. It remains unclear whether formation rates and locations of peak activity change over decadal or centennial timescales.

Slope streak count data are openly available here: <https://doi.org/10.48620/91828>.

Seismicity as a non-seasonal driver of streak formation

Two of the twenty-four (~8%) InSight-recorded BB and LF events with back-azimuth-derived epicenter locations ('Broadband' and 'Low-Frequency', MQS Catalog v14)^{20,21} feature – more or less distinct – bursts of newly formed streaks in post-quake images acquired of the reconstructed epicenter location: events S0105a, moment magnitude (M_w) 3.0 (2019-03-14, 10 new streaks), and S0173a, M_w 3.7 (2019-05-23, 15 new streaks), both located in Elysium. This implies that endogenic seismicity can trigger streak formation, although the current data imply that the contribution to the global formation budget might be small: assuming the 25 identified, newly formed streaks formed within one Mars Year, tectonic activity might be responsible for as little as ~0.04% of the streaks that form on Mars every MY. Importantly, the InSight data are spatiotemporally scarce, cover only ~2 MY and a small fraction of the planet, and thus do not allow for an extended comparison with the global-scale slope streak formation data. Further, the inaccuracies associated with the spatial localization of quake epicenters are substantial (e.g., ref. 22), and a direct relation between a quake and newly formed streaks is difficult to (dis)prove, particularly with image pairs that were acquired weeks and months apart. In reality, endogenic seismicity might be a substantially more important driver of streak formation than suggested by the results above.

An association of newly formed meteoroid impacts and streaks is more straightforward (Fig. 2A–E). Overall, 254 of the 1027 cells (~25%) with impact craters that formed during CTX operations²³ host slope streaks and are covered with at least 2 CTX images that meet the desired change detection requirements. Of those 254 cells, 14 cells (~6%) show bursts of newly formed streaks in post-impact images. In total, impact events appear to have triggered the formation of 255 (CTX-scale) slope streaks between 2006 and 2020, implying that impact events lead to the formation of an average of ~34 slope streaks per MY, or about ~0.05% of the annual formation population.

This analysis does not include two specific streak bursts that recently have been tied to seismicity by Bickel and Valantinas⁷ and Lucas et al.²⁴: S1000a (impact) and S1222a (quake). S1000a is not part of Daubar et al.'s²³ global database, and the cells around S1222a's current epicenter location (covering ~2000 km²) host a minimal number of slope streak detections (<10), which removes both events from my analysis.

Dust, wind action, and saltation as seasonal drivers of streak formation

The difference count data and modeled, low-resolution, regional-scale atmospheric data extracted from the Mars Climate Database (MCD v6.1)²⁵ suggest that ~20% of the cells with ongoing (directly observed) streak formation activity experience wind stress values beyond 0.02 Pa (maximum of the sol at image pair mean L_S , with a maximum temporal difference of 6 months or 90° L_S between the images). Here, wind stress values are estimated from horizontal wind velocities (modeled

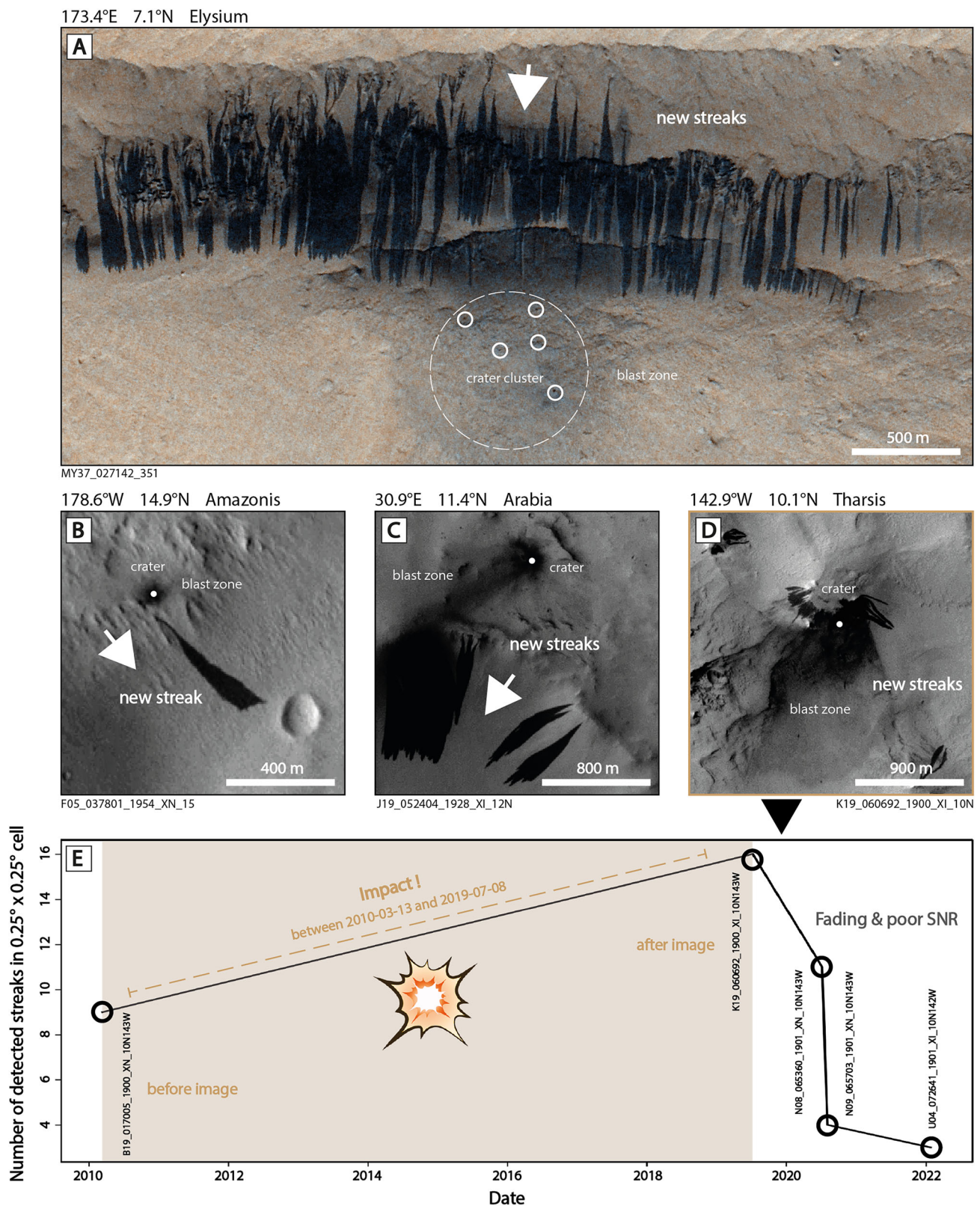


Fig. 2 | Meteoroid impacts as drivers of non-seasonal (burst) streak formation. **A** new impact crater cluster that formed in Elysium and triggered a slope streak burst with more than 100 individual (CaSSIS-scale; Colour and Stereo Surface Imaging System)⁶⁷ streaks; image credits ESA/TGO/CaSSIS CC-BY-SA 3.0 IGO; note that CaSSIS has a higher spatial resolution than CTX. Additional observations of impact events that triggered streak formation as imaged by CTX in Amazonis (**B**), Arabia (**C**), and Tharsis (**D**); crater location indicated by white point; image credits

NASA/MSSS/ASU. Downslope direction indicated by white arrow, where appropriate. **E** History of slope streak counts for all considered CTX image pairs for the cell shown in (**D**) ($n = 4$, with 5 images), between 2010 and 2022; the impact happened anytime between 2010-03-13 and 2019-07-08 (indicated by beige shading); the drop of the streak count after the impact can be attributed to a combination of streak fading and illumination/SNR (signal to noise) issues of the following images.

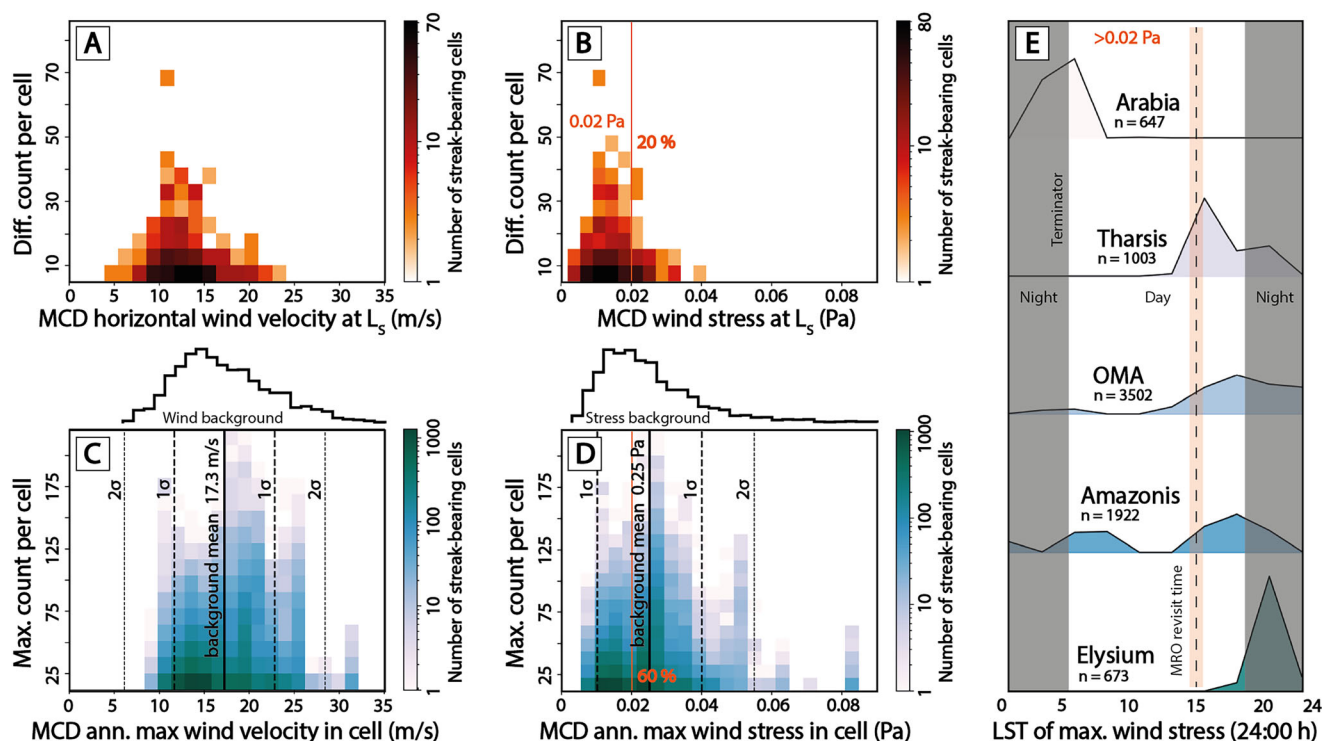


Fig. 3 | Evidence for wind action as one of the drivers of streak formation magnitude. Relation of streak count difference and modeled MCD sol-maximum (regional, averaged) horizontal wind velocity 4.5 m above the surface (A) and estimated wind stress (B), at the L_s of the count difference measurement (maximum of the sol at image pair mean L_s); ~20% of all cells that experienced streak formation exceed estimated wind stress values of 0.02 Pa (indicated by vertical red line). Relation of streak maximum count and modeled MCD annual-maximum (regional, averaged) horizontal wind velocity 4.5 m above the surface (C) and estimated wind stress (D); ~60% of all streak-bearing cells exceed estimated wind

stress values of 0.02 Pa. E Joyplot (showing counts) of the LST at which (MCD-based, regional) diurnal maximum wind stresses occur at the five main streak populations, only considering values with associated wind stress values >0.02 Pa; day- (white shade) and night-side (black shade) indicated; MRO's orbital revisit time (centered at ~3 PM) indicated by vertical dashed line and beige shade. The number of cells considered per region is indicated. Background distribution of (modeled) maximum annual wind velocity and stress (for all cells, $n = 520,200$) visualized by black histograms in (C) and (D); black vertical lines represent the background distribution's mean (thick line) and 1σ , 2σ (dashed line).

at 4.5 m above the surface) and the spatiotemporally associated atmospheric density, assuming a simplified aerodynamic (surface) roughness of 2 centimeters. Throughout the year, ignoring streak formation timing, about ~60% of all streak-bearing cells experience peak wind stress values beyond 0.02 Pa (Fig. 3B, D). Several past studies suggested that wind stress in excess of 0.02 Pa is able to initiate and sustain the saltation of sand-sized particles (~100 μm) that are the most susceptible to wind shear (e.g., refs. 26–34). Upon re-impact on the surface, these particles can mobilize and eject smaller particles, including dust particles (<62 μm), making wind stress values beyond 0.02 Pa indicative of atmospheric conditions that are generally conducive to the mechanical triggering of streak formation. Generally, the average sol-maximum wind stress in streak-bearing cells tends to approach or exceed 0.02 Pa at around L_s -220°, in early southern summer (Fig. 4E, F), agreeing with the observed surge in streak formation activity (Fig. 1B). Notably, cells with faster near-surface winds and higher wind stresses tend to experience higher streak formation rates (Fig. 3), but that effect seems to vanish for wind velocities and wind stress values beyond ~12 to ~17 m/s (at an altitude of 4.5 m) and ~0.02 to ~0.03 Pa (Fig. 3). These spatiotemporal observations suggest that wind action, or more specifically, wind stress-induced saltation, is a major driver of streak formation. Importantly, MCD-predicted atmospheric parameters represent regional averages and are not expected to fully capture the dynamics of the atmosphere at the slope streak scale, which directly affects all estimates of wind stress. In addition, the assumed, simplified (constant) aerodynamic roughness cannot be expected to fully capture the variability of surface roughness across Mars.

The local times at which modeled maximum wind stresses occur (excluding wind stress values below 0.02 Pa) vary substantially across the five geographic streak hotspots: in Arabia, the conditions most conducive to streak formation appear to occur at sunrise; in Tharsis, these conditions appear in the late afternoon; in Amazonis, the most conducive wind stresses occur shortly after sunrise and shortly before sunset; and in OMA and Elysium, these conditions appear at and shortly after sunset (Fig. 3E). These observations might explain why direct observations of actively forming streaks – and potentially associated dust clouds or plumes – have not been made over the past decades of Mars imaging, as the vast majority of orbiters were constrained to imaging around noon and the early afternoon – and as only a few orbiters are capable of sunrise and sunset imaging, such as ESA's Trace Gas Orbiter and Mars Express.

My data also suggest that 92% of all difference and maximum count cells are located in regions featuring very high TES albedo (>0.26, Fig. 5A, C), with ~99% of all streak-bearing cells exceeding the average surface albedo (across all analysis cells). Notably, higher surface albedo seems to lead to higher formation rates and maximum streak counts. Similarly, MCD-derived column-integrated dust optical depth values of cells with active (directly observed) streak formation (maximum of the sol at image pair mean L_s , with a maximum temporal difference of 6 months or 90° L_s between the images, Fig. 1F) as well as the sol-maximum dust optical depth of streak-bearing cells in general (Fig. 4A, B), show an enhanced atmospheric dust load during the seasons that are associated with streak formation activity, with a distinct rise at L_s -220°, coinciding with streak formation activity (Fig. 1B). Notably, the sol-maximum dust optical depth at cells that experience

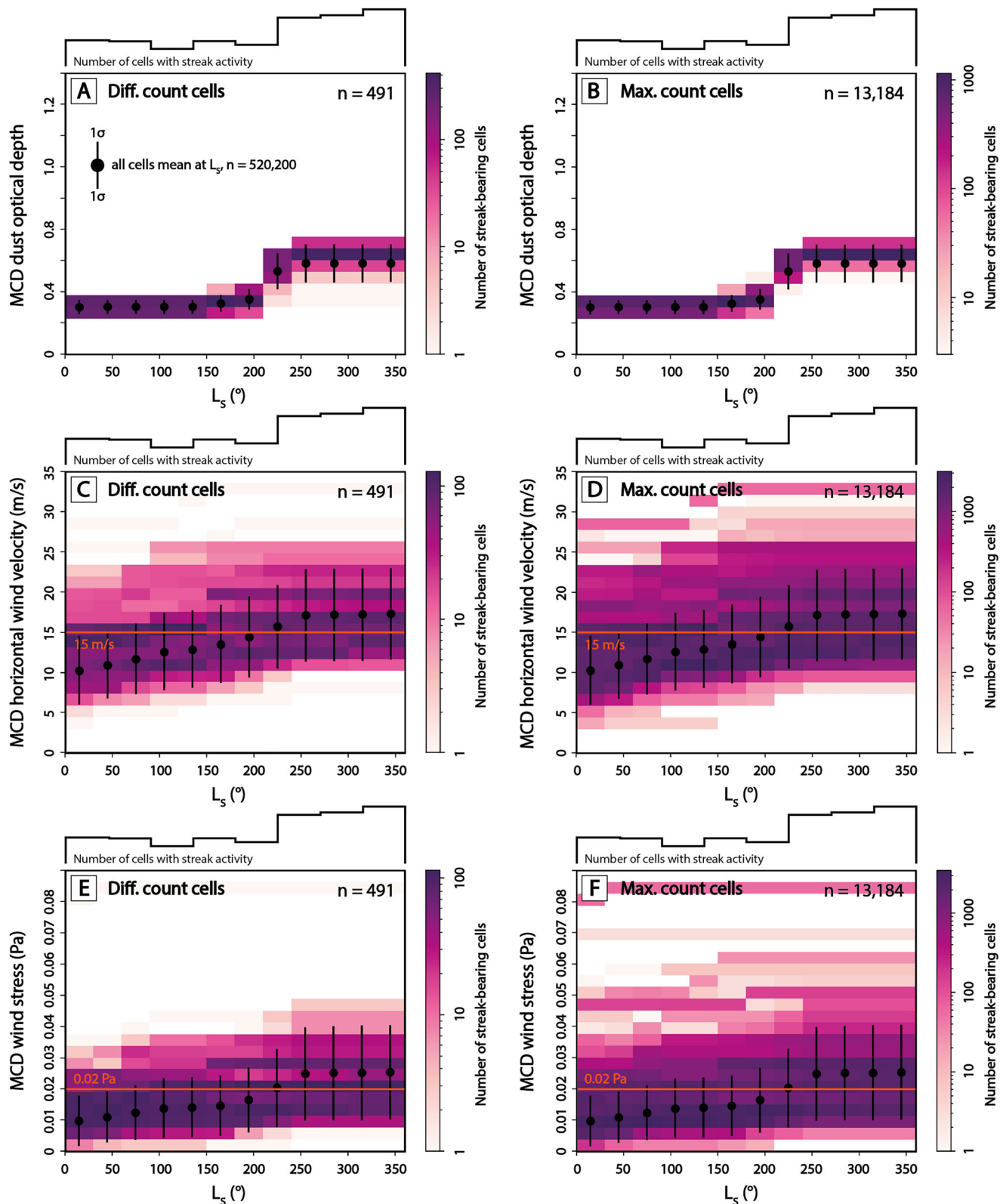


Fig. 4 | Evidence for wind action and atmospheric dust as key drivers of streak formation seasonality. MCD dust optical depth (A, B), modeled (regional, averaged) MCD sol-maximum horizontal wind velocity (4.5 m above the surface) (C, D), and estimated sol-maximum wind stress (E, F) as a function of L_s (season), for all cells that host difference counts (left column, $n = 491$) and maximum counts (right column, $n = 13,184$). The mean and standard deviation of the properties of all

analysis cells ('background', $n = 520,200$) are overlain as black dots and vertical lines, respectively. Background distribution of slope streak formation activity is indicated by a black histogram above each panel; note that this histogram does not consider the magnitude of formation (i.e., counts), as visualized in Fig. 1B. The horizontal red lines highlight wind velocities and wind stress values beyond 15 m/s and 0.02 Pa in (C–F).

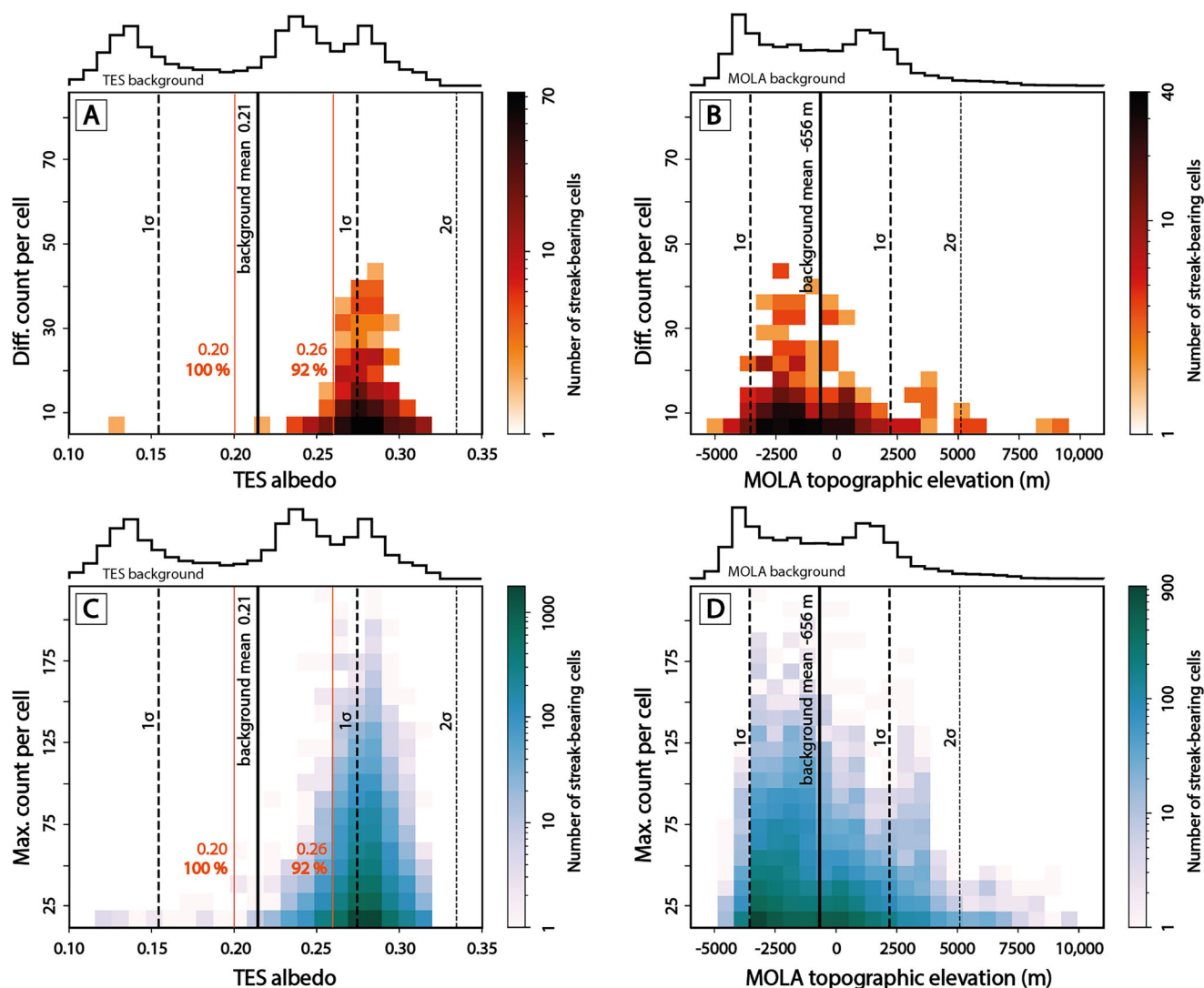


Fig. 5 | Evidence for dust as a key pre-conditioning factor for streak occurrence and a key driver of streak formation magnitude. Relation of streak count difference and TES (Thermal Emission Spectrometer) albedo (A) and MOLA (Mars Orbiter Laser Altimeter) topographic elevation (B); 92% and 100% of all cells that experienced streak formation exceed an albedo of 0.26 or 0.20 (marked by red vertical lines), respectively, indicative of the abundance of fine dust. Relation of

streak maximum count and TES albedo (C) and MOLA topographic elevation (D); 92% and 100% of all streak-bearing cells exceed an albedo of 0.26 or 0.20 (marked by red vertical lines), respectively. Background distribution (for all cells, $n = 520,200$) visualized by black histograms; black vertical lines represent the background distribution's mean (thick line) and 1 σ , 2 σ (dashed line).

streak formation and/or host slope streaks remains slightly above the background over the course of southern summer and fall, i.e., during streak formation season (Fig. 4A, B). Further, peak streak activity – and streak abundance in general – appears to be centered at elevations of ~2000 to ~2500 m (Fig. 5B, D), below the average background. Figure 6 visualizes the interaction between the key drivers of streak occurrence, where all streak-bearing cells are located in high-albedo (dust-rich) terrain and at lower topographic elevations, with a distinct indication that higher albedo and lower elevations generally result in enhanced streak activity (for difference and maximum counts). Figure 6 also underlines the direct relation between streak activity, wind velocity, and wind stress, where regions of peak activity correspond to regions of enhanced wind action.

Discussion

My observations highlight how the interaction of three key pre-conditioning factors and drivers lead to seasonal slope streak activity: (1) the presence of topographic inclines, (2) a combination of surface dust and the seasonal delivery of atmospheric dust, as well as (3) the

mechanical mobilization of dust through saltation, which in turn is driven by near-surface winds and the atmospheric density. All three preconditions and drivers are required to form slope streaks. The data suggest that the wind stress at slope streak-bearing locations is not necessarily higher than elsewhere on Mars but seems to be high enough (>0.02 Pa) to initiate and sustain the saltation of sand-sized particles (~ 100 μ m) and – with that – the mobilization of dust particles. On inclined terrain, the local mobilization of sand and dust can lead to a cascading effect and the formation of slope streaks.

This mechanism highlights the seemingly important role of another key factor, the availability of sand-sized particles (in the ~ 100 μ m range), which are the most susceptible to wind stress and, thus, are the most likely to trigger downslope dust displacement through saltation. Notably, past surveys established that aeolian features, which imply the presence of loose sand, such as (Barchan) dunes and ripples, are widespread across Mars^{35,36}, including all the geographic slope streak hotspots identified in this work. Other surveys established that sand migration is strongly seasonally controlled as well and surges in early southern summer, remaining high throughout

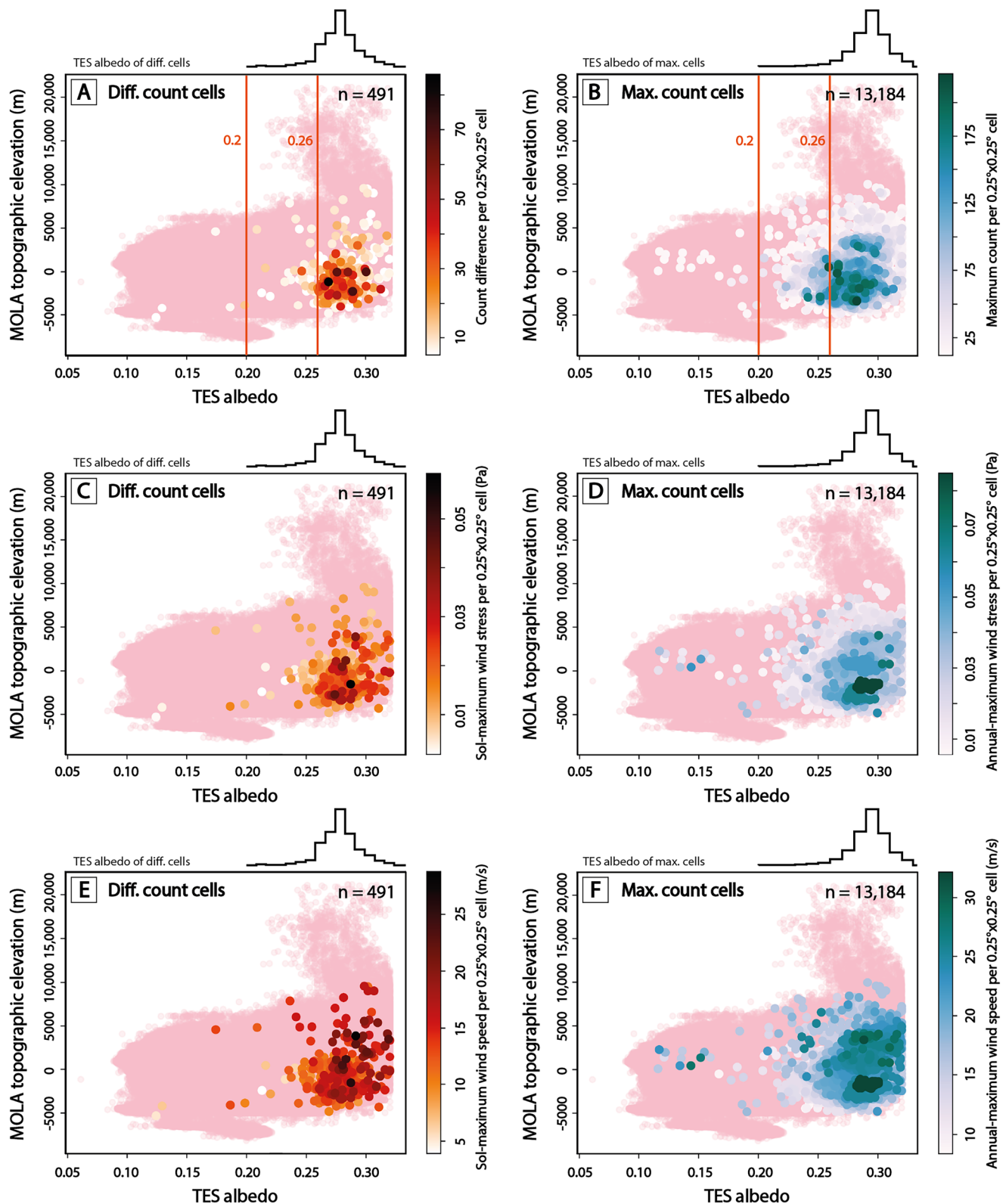


Fig. 6 | Dust abundance and wind action as the main drivers of streak formation. Relation of MOLA (Mars Orbiter Laser Altimeter) elevation and TES (Thermal Emission Spectrometer) albedo for all difference count cells (left column, A, C, E) and maximum count cells (right column, B, D, F), in comparison to all analysis cells ($n = 520,200$, transparent coral color, in the background); the difference and maximum count data are colorized using count difference or maximum count per

cell (A, B), (estimated) sol-maximum or annual-maximum wind stress per cell (C, D), and (modeled) sol-maximum or annual-maximum wind velocity per cell (E, F). Red vertical lines in (A, B) indicate albedo values highlighted in Fig. 1 and Fig. 5, indicative of the abundance of fine dust. TES albedo distribution for difference and maximum count cells ($n = 491$, $n = 13,184$, respectively) visualized by black histograms.

southern autumn (e.g., refs. 27,37,38). This implies that the spatial distribution of sand as well as the periodicity and magnitude of sand migration closely agree with the distribution and activity of slope streaks, directly supporting the hypothesis that dust, wind, and (saltating) sand jointly drive slope streak formation on Mars.

Importantly, all estimates of wind stress are based on several assumptions, such as the utilization of one average, simplified (and potentially too high) aerodynamic roughness for the entire surface of Mars. These assumptions follow several preceding studies (e.g., refs. 34,39) but are likely to affect the overall accuracy of the derived wind stress estimates, also because of the low spatial resolution of the MCD. Notably, a recent study that used the movements of dust devils to measure near-surface wind velocities across Mars³⁴ suggests that the global-scale MCD – not surprisingly – systematically and substantially underestimates local-scale wind velocities, suggesting that the wind stresses at streak locations could be larger than estimated here, further underscoring the ability of near-surface winds to initiate sand saltation and trigger streak formation. As highlighted by Bickel and Valantinas⁷, future studies of slope streak formation and activity should utilize atmospheric meso-scale models and a wider range of aerodynamic roughness values – in combination with the new slope streak dataset that is associated with this study – to address some of the key shortcomings of this study.

In contrast to seasonal drivers, meteoroid impacts and quakes seem to be locally distinct, yet globally relatively insignificant drivers of slope streak formation, which might help explain why Bickel and Valantinas⁷ only observed a weak statistical (purely spatial) relation between impact and streak locations, and only in Arabia Terra. Similarly, other local studies only found modest evidence for a potential impact of the strongest recorded marsquake (S1222a) on regional streak formation rates²⁴. Notably, impact-generated and endogenic seismicity are (predominantly) non-seasonal and appear to primarily drive bursts of streak formation, which seem to exceed the rates commonly observed for seasonal drivers like wind action and saltation (Fig. 1B). This distinction might make the detection of very large (off-season) streak bursts – in the absence of newly formed impact craters – a powerful tool for the orbital, global monitoring of Mars' present-day tectonic activity, at least in the dust-covered, topographically rough regions of the northern hemisphere.

For example, my workflow identified a number of very large streak formation bursts that cannot be associated with impact events or seasonal wind action and saltation, such as in Amazonis, southern Erebus Montes (170.7°W, 24.1°N), where more than 270 streaks formed within four adjacent $0.25^\circ \times 0.25^\circ$ cells, across tens of kilometers – and numerous more streaks across other cells in the vicinity, between 2008-01-07 and 2013-09-25. This burst occurred pre-InSight and it is unclear whether it was indeed triggered by tectonic activity or whether it might be tied to the 2007 planet-encircling dust storm⁴⁰; if this burst was caused by a marsquake, its magnitude appears to have exceeded the $3.3 M_w$ of S1222a, the strongest recorded marsquake⁴¹, judging from the pronounced difference in the number of new streaks and the extent of their spatial distribution. The utilization of very large streak bursts for the detection of tectonic activity remains an intriguing possibility, highlighting the imperative role of orbital assets that can provide long-term, continuous, global-scale, and intermediate-resolution (space and time) observations of the martian surface, such as currently provided by MRO and other orbiters, and as envisioned by ESA's Lightship (and Spotlight) concept for the future^{42,43}.

Using measures of average streak area (0.1 km^2) and assumptions about average streak thickness (5 cm, based on refs. 8,44) and dust density (2500 kg/m^3), streak formation as described by a conservative, normalized long-term formation rate ($\sim 4.2\%/MY$) would imply the displacement of a dust volume of $\sim 3.4 \times 10^{-1} \text{ km}^3/MY$, $\sim 3 \times 10^{-1} \text{ km}^3/MY$ of which might potentially get injected into the atmosphere ($\sim 90\%$, per, e.g., refs. 8,45), representing a dust mass of about $\sim 7.6 \times 10^8 \text{ t/MY}$,

corresponding to $\sim 26\%$ of the global, annual surface-to-atmosphere exchange budget (per ref. 46) or ~ 1.9 global dust storm equivalents (per ref. 47). Currently, TGO's CaSSIS instrument is attempting to capture the active formation of slope streaks and verify the existence of associated dust plumes. Direct observations are required to verify or discard the potentially critical role of slope streaks in the martian dust cycle – and quantify their specific contribution to the surface-to-atmosphere exchange budget.

Methods

Few-shot learning-driven slope streak mapping

I build on the validated slope streak detector (based on YOLOv5, PyTorch 1.7, from <https://github.com/ultralytics/yolov5>) used in ref. 7 and substantially improve its overall detection performance by adding a total of 4737 and 389 new slope streak labels located in a total of 575 and 41 CTX image patches (1000×1000 pixels each), for training and testing data, respectively, taken from 27 CTX images. The full, used training and testing datasets include 5744 and 424 streak labels taken from 68 CTX images. Each label represents one rectangular bounding box drawn around a slope streak. Data selection, labeling, and validation, as well as detector training, follow the identical procedures as documented by Bickel and Valantinas⁷, including label augmentation (label rotation, up-down flipping, shearing, scaling, and contrast/brightness modifications), which in turn followed established procedures. All used CTX images are listed in Table S1.

The trained detector achieves a recall of $\sim 75\%$ (% streaks in testset identified) and a precision of $\sim 94\%$ (% correctly identified testset streaks) at a model confidence threshold of 0.5, with an AP (average precision) of $\sim 80\%$. The detectors used by Bickel and Valantinas⁷ and in this work cannot be directly compared due to their different testsets, but the performance of the new detector is expected to be substantially enhanced, due to the considerably larger and more diverse trainset. The test results imply that the detector is able to identify about 75% of all streaks visible in a CTX image, while about 94% of its detections are correct, on average. For this study, I deploy the new detector with a confidence threshold of 0.5, i.e., I consider all detections with model confidence scores higher than 0.5. Due to the fact that individual streaks can be spatially co-located or overlap (nested streaks), I use a random set of 1000 streaks to estimate the average number of slope streaks per detection: ~ 2 (slightly lower than the ~ 2.33 estimated by Bickel and Valantinas⁷, most likely due to the improved detector).

The deployment of the detector uses the identical methodology as detailed in ref. 7, utilizing one single NVIDIA RTX 3090 GPU (Graphical Processing Unit) and a processing pipeline developed over several years (e.g., refs. 48,49). The workflow retrieves map-projected and calibrated CTX images located between 55°N and 35°S ($n = 105,754$, geographically constrained by the earlier global census conducted by Bickel and Valantinas⁷) from <https://image.mars.asu.edu/stream/>, cuts them into 1000×1000 pixel patches, deploys the detector, and uses the standard YOLOv5 NMS (non-maximum suppression) to remove duplicate detections made in the same image patch, as is best practice for object detection. All detections are stored along with preview thumbnails and CTX-derived metadata, such as accurate geographic location, image solar longitude, image ID, image acquisition date, illumination conditions, and imaging geometry. Total processing of the entire (available) CTX image archive required ~ 1.5 months using one single GPU-enabled desktop computer. The detector identified a total of 2,169,234 individual slope streak detections, which are too many for a manual candidate review, as performed by Bickel and Valantinas⁷; in this study, I rely on the thorough (statistical) assessment of the precision of the detector in the testset: this assessment suggests a precision of 94%, which means that a minimal number of false detections are included in the dataset, but strongly implies that those false detections will not have any substantial effect

on the scientific results and interpretations. A purely statistical assessment of detector precision – without manual review – is common for datasets with extremely large numbers of detections, such as recently showcased in ref. 50, which mapped millions of boulders across the lunar surface.

Spatiotemporal data binning and statistics

I use a geographic grid consisting of 520,200 $0.25^\circ \times 0.25^\circ$ quadrangles that cover Mars between 55°N and 35°S . Each slope streak detection is associated with the unique ID of its ‘host cell’ or ‘analysis cell’. The spatiotemporal analysis is conducted on a cell-by-cell basis. Overall, I consider 91,687 CTX images. On average, each analysis cell intersects with 6.52 CTX images, with a minimum of 1 image and a maximum of 187 images. The used CTX images feature a homogeneous longitudinal distribution and a relatively homogeneous latitudinal distribution, with fewer images taken at very high northern latitudes, beyond -45°N (Fig. S3). Past surveys have not identified any slope streaks at latitudes beyond -40°N (e.g., ref. 7). The used CTX images feature a slightly heterogeneous seasonal distribution, with more images acquired over northern spring and summer ($L_S - 0^\circ$ to -170°) and fewer images over southern spring, summer, and autumn ($L_S - 220^\circ$ to -360°) (Fig. S3). The relative lack of images is particularly expressed at very high northern latitudes, beyond -40°N , between -200° and $-360^\circ L_S$, where no slope streaks are present. It is unlikely that the seasonal imbalance of images has an effect on the results of this study, as the overabundance of images in northern spring and summer should affect the streak counts at those seasons, yet the peak streak formation season is associated with southern spring, summer, and autumn (Fig. 1B).

Maximum counts

This workflow uses the slope streak counts made by the detector in a given cell, in all CTX images that fully or partially overlap that cell. The workflow selects the overall maximum count made in each cell; in other words, the workflow derives the largest number of slope streaks ever recorded by CTX in a given cell. In addition, the workflow extracts the maximum (annual) climatology average solar MY horizontal wind velocity (U_x) at an altitude of 4.5 m above the surface (z), a daily column-integrated dust optical depth value (regularly kriged maps of $9.3\text{ }\mu\text{m}$ absorption column dust optical depth, 610 Pa⁵¹), as well as the atmospheric density (ρ_a) at the respective time from the MCD^{25,52}. I use those parameters along with the law of the wall³³ to compute the wind shear velocity (u_*) at surface level (with κ as the von Kármán constant, 0.4, and z_0 as the aerodynamic surface roughness, here 2 cm):

$$\overline{U_x}(z) = \frac{u_*}{\kappa} \ln\left(\frac{z}{z_0}\right) \quad (1)$$

and then estimate the wind stress (τ) using^{28,33}:

$$\tau = \rho_a * u_*^2 \quad (2)$$

z_0 is computed using (per, e.g., ref. 39):

$$z_0 = 2 * \frac{D}{30} \quad (3)$$

assuming a median grain size (D) of 30 cm, as recently used by Bickel et al.³⁴. I note that the utilization of one single D and z_0 value as well as the usage of Eq. (3) largely oversimplifies the substantial variability of the aerodynamic roughness across Mars. Most notably, the assumed D and z_0 values are relatively high and might not be fully representative for many slope streak-bearing regions.

Wind stress values beyond -0.02 Pa , either vortical (e.g., in dust devils or convective vortices)^{53–55} or non-vortical (e.g., in near-surface wind gusts)^{28,34} have been shown to be able to initiate and sustain the

saltation of sand-sized particles ($\sim 100\text{ }\mu\text{m}$), which can eject finer dust-sized particles upon re-impact on the surface. The ejection of dust through saltating sand-sized particles is suspected to be the main dust lifting mechanism on Mars (e.g., ref. 33,56–60). Lastly, the workflow extracts the TES albedo⁶¹ and MOLA topographic elevation^{62,63} at each streak location.

Differential counts - seasonal

This workflow selects all CTX images that have a 100% overlap with a given cell, i.e., the process excludes images that might only partially cover a given cell, which likely leads to lower counts. Subsequently, the workflow identifies image pairs with a temporal acquisition difference of less than 6 months (one quarter MY, $90^\circ L_S$), counts slope streaks in the before and after image, and computes a count difference, embodying an integration of the number of streaks that formed and faded between the two images. I identify 6 months as the most appropriate time difference (time window) for this analysis, as it represents the best compromise between data availability and temporal resolution, i.e., identified changes can be attributed to a season with reasonable accuracy – yet, the temporal window is wide enough to maximize the number of image pairs available, which in turn improves the overall spatiotemporal coverage of the analysis.

The slope streak counts can be substantially affected by the illumination and observation geometries of the available images, as well as their overall data quality and the state of the Martian atmosphere (e.g., atmospheric dust, Fig. 1C, D, S1). In fact, the conditions that mainly drive detections of false changes (solar incidence and atmospheric dust) are more prevalent during the southern summer and fall, which might affect the results of the presented change detection analysis. I carefully characterize the noise floor caused by false changes in a statistical manner by comparing detector- and human-derived (ground-truth) streak counts in 100 control cells across the five streak hotspots. The median absolute difference between detector- and human-derived change counts (i.e., counts of newly formed streaks) is 4 per cell per pair (Fig. 1C). As the total number of streaks per cell can vary drastically and as streaks can be nested, I define the noise floor as the median percentage of the difference between the human-derived count difference and the detector-derived count difference and the mean of the detector-derived before and after image counts, i.e., $\sim 24\%$ (Fig. 1D). This study only considers difference counts that exceed the median noise floor, to minimize the impact of false changes, acknowledging that the application of the noise floor reduces the overall sensitivity of the investigation to subtle, small-scale changes. Importantly, even changes beyond the noise floor can be caused by data quality issues or differences (Fig. 1C, D), which remains the most relevant limitation of the overall accuracy of the presented results. Notably, tightening the requirements on, for example, incidence and temporal differences between CTX images drastically reduces the overall number of cells with appropriate spatiotemporal coverage, impeding a representative, global-scale change detection analysis (Fig. 1G). My analysis does not consider the fading of slope streaks (negative formation rates), as the signature of fading streaks is less clearly defined (i.e., is not binary, as in the streak formation case, e.g., ref. 12) and is thus substantially less pronounced in the count data, and is also noticeably more affected by count noise.

For all cells with slope streaks, the workflow further uses the average L_S of a given image pair to extract a daily column-integrated dust optical depth value (regularly kriged maps of $9.3\text{ }\mu\text{m}$ absorption column dust optical depth, 610 Pa) from the MCD⁵¹. The workflow also extracts the maximum (regional, averaged) horizontal wind velocity value (at an altitude of 4.5 m above the surface) that is predicted by the MCD for the given sol, at the given L_S and the given MY, as well as the corresponding atmospheric density value^{25,52}. As for the maximum count workflow, I use those parameters to compute the wind shear velocity at the surface level and to estimate the resulting wind stress.

As a last step, the workflow extracts the TES albedo⁶¹ and MOLA topographic elevation⁶² at all streak locations.

Differential counts – non-seasonal

This workflow focuses on all cells that contain (a) slope streaks and (b) a new impact that formed during CTX operations ($n = 1027$, based on ref. 23) or an InSight epicenter location ($n = 24$, BB ‘Broadband’ and LF ‘Low-Frequency’ events with back-azimuth, InSight MQS Catalog v14)^{20,21}. InSight BB and LF events are classified as tectonic events^{41,64}. If a cell contains a quake epicenter, all adjacent 8 cells are also included in the analysis, to broaden the spatial footprint of the overall analysis. The workflow considers all CTX images that overlap a given cell at least by 90%, counts slope streaks in each image, and plots all counts as a function of time (Fig. 2E), along with the temporal brackets derived by Daubar et al.²³ for each impact event – or along with the exact timing of a given quake, as provided by the MQS Catalog v14²⁰. The utilization of a 90% overlap criterion slightly increases the count noise but substantially increases the number of images available for the analysis. I manually analyze each of the cell time-series, looking for subtle to stark increases in the streak counts that could be related to an impact or seismic event.

Manual ground-truth counts

In order to validate all automated maximum and difference counts, I conduct a detailed manual slope streak time-series analysis of two separate cells centered at 24°N, 147°W and 28°N, 145°W, in OMA. The analysis uses a total of 40 and 26 CTX image pairs, respectively, that feature 100% overlap with the cell and feature temporal differences of less than 6 months, acquired as part of a monitoring campaign between 2007 and 2023. This workflow resembles the differential count workflow, (manually) counts slope streaks in before and after images, per image pair, computes count differences, and records them along with the average L_s of the respective CTX image pair (Fig. 1B).

Formation rates

I use an adapted workflow to derive slope streak formation rates on MY-scales. This workflow utilizes all CTX images that have a 100% overlap with a given cell, selects the two images with the largest temporal difference (with a maximum difference of -17 years or -8.5 MY, -2007 to -2024), counts slope streaks in the before and after image, and computes the count difference. The workflow uses two approaches to compute slope streak formation rates: (1) one approach relates the number of streaks that formed between the before and after image to their temporal difference, providing a measure of ‘newly formed slope streaks per MY’ (N_c):

$$N_c = \frac{N_{diff\ count}}{\Delta_t} \quad (4)$$

Notably, the number of newly formed streaks is dependent on the overall abundance of slope streaks in a given cell (see, e.g., ref. 15), which is why approach (2) relates each difference count to the total number of slope streaks that are present in the after image (N_{total}), providing a measure of ‘percentage of population-increase per MY’ (N_n), directly following the methodology developed and used by^{12,16–18}:

$$N_n = \frac{N_{diff\ count}}{\Delta_t * N_{total}} * 100 \quad (5)$$

Methodological and data limitations

The most important limitation of the accuracy of the presented results is the noise caused by (a) the slope streak counts and (b) the temporal bias introduced by the applied CTX image pair window (6 months),

which in turn are rooted in the variability of the available CTX image data, as discussed above. In addition, there are other factors that affect the accuracy of the results presented throughout this work. The spatiotemporal analysis relies on various auxiliary datasets and model-derived products, specifically, TES surface albedo⁶¹, MOLA topographic elevation^{62,63}, catalogs of new impact craters²³ and marsquakes^{20,21}, and the MCD^{25,52}. Each of those products is subject to different limitations that might affect the results of this study. For example, the used catalogs of new impacts and marsquakes are very likely incomplete, in space and time, as demonstrated by recent studies that identified additional impact events (see, e.g., ref. 65). InSight data, in particular, is extremely scarce in space and time, and only features minimal overlap with the other datasets used. TES and MOLA products feature spatial resolutions that are not representative of the local, meter-scale environment that is likely to play an important role in slope streak pre-conditioning and triggering. The MCD only provides approximate, low-resolution, region-scale (5.625° longitude by 3.75° latitude per cell), and thus heavily averaged insights into atmospheric processes, and cannot be expected to fully represent the dynamic, complex topographic environments slope streaks are located in. Recent work showed that the MCD appears to substantially underestimate the horizontal near-surface wind velocity³⁴, which implies that this work underestimates the wind stresses at slope streak locations. I underline the importance of local and regional studies – and the utilization of high-resolution products and meso-scale atmospheric models, in combination with the new dataset that is associated with this study – for the future verification and scrutiny of the results presented here, as previously highlighted by Bickel and Valantinas⁷.

Data availability

This work is exclusively based on open data. The slope streak count data generated in this study have been deposited in the University of Bern’s BORIS database under accession code: <https://doi.org/10.48620/91828>⁶⁶. InSight seismic data is available here: <https://www.insight.ethz.ch/seismicity/catalog/v14>. CaSSIS image data are openly available here (use the search bar to find specific image IDs or zoom and pan on the map): <https://observations.cassis.unibe.ch/>. HiRISE data are openly available here: <https://www.uahirise.org/>. CTX image data are openly available here: <https://viewer.mars.asu.edu/viewer/ctx#T=0>. The used USGS map products (MOLA topography, TES albedo) are openly available here, respectively: (1) https://astrogeology.usgs.gov/search/details/Mars/GlobalSurveyor/MOLA/Mars_MGS_MOLA_DEM_mosaic_global_463m/cub, (2) https://astrogeology.usgs.gov/search/map/Mars/GlobalSurveyor/TES/Mars_MGS_TES_Albedo_mosaic_global_7410m.

Code availability

This work is exclusively based on open software. The used YOLOv5 architecture is openly available here: <https://github.com/ultralytics/yolov5>.

References

1. Morris, E. Auerole deposits of the martian volcano Olympus Mons. *J. Geophys. Res. Planets* <https://doi.org/10.1029/JB087iB02p01164> (1982).
2. Ferguson, H. & Lucchitta, B. Dark streaks on talus slopes, Mars. In *Planetary Geology and Geophysics Program Report* 188–190 <https://ntrs.nasa.gov/citations/19840015431> (1984).
3. Bhardwaj, A., Sam, L., Martin-Torrez, F., Zorzano, M.-P. & Fonseca, R. Martian slope streaks as plausible indicators of transient water activity. *Nat. Sci. Rep.* <https://doi.org/10.1038/s41598-017-07453-9> (2017).
4. Kreslavsky, M. & Head, J. Slope streaks on Mars: a new “wet” mechanism. *Icarus* <https://doi.org/10.1016/j.icarus.2009.01.026> (2009).

5. Schorghofer, N., Aharonson, O. & Khatiwala, S., Slope streaks on Mars: correlations with surface properties and the potential role of water. *Geophys. Res. Lett.* <https://doi.org/10.1029/2002GL015889> (2002).
6. Ferris, J., Dohm, J., Baker, V. & Maddock, T. Dark slope streaks on Mars: are aqueous processes involved? *Geophys. Res. Lett.* <https://doi.org/10.1029/2002GL014936> (2002).
7. Bickel, V. & Valantinas, A. Streaks on Martian slopes are dry. *Nat. Commun.* <https://doi.org/10.1038/s41467-025-59395-w> (2025).
8. Dundas, C. Geomorphological evidence for a dry dust avalanche origin of slope streaks on Mars. *Nat. Geosci.* <https://doi.org/10.1038/s41561-020-0598-x> (2020).
9. Dundas, C. et al. Granular flows at recurring slope lineae on Mars indicate a limited role for liquid water. *Nat. Geosci.* <https://doi.org/10.1038/s41561-017-0012-5> (2017).
10. Heyer, T., Raack, J., Hiesinger, H. & Jaumann, R. Dust devil triggering of slope streaks on Mars. *Icarus* <https://doi.org/10.1016/j.icarus.2020.113951> (2020).
11. Vincendon, M., Pilorget, C., Carter, J. & Stcherbinine, A. Observational evidence for a dry dust-wind origin of Mars seasonal dark flows. *Icarus* <https://doi.org/10.1016/j.icarus.2019.02.024> (2019).
12. Stillman, D., Hoover, R., Kaplan, H., Fenton, L. & Primm, K. Comprehensive observations and geostatistics of slope streaks within the Olympus Mons Aureole. *Icarus* <https://doi.org/10.1016/j.icarus.2024.116061> (2024).
13. Dickson, J., Ehlmann, B., Kerber, L. & Fassett, C. The Global Context Camera (CTX) mosaic of Mars: a product of information-preserving image data processing. *Earth Space Sci.* <https://doi.org/10.1029/2024EA003555> (2024).
14. Malin, M. et al. Context camera investigation on board the Mars Reconnaissance Orbiter. *JGR Planets* <https://doi.org/10.1029/2006JE002808> (2007).
15. Aharonson, O., Schorghofer, N. & Gerstell, M. Slope streak formation and dust deposition rates on Mars. *J. Geophys. Res. Planets* <https://doi.org/10.1029/2003JE002123> (2003).
16. Heyer, T. et al. Seasonal formation rates of martian slope streaks. *Icarus* <https://doi.org/10.1016/j.icarus.2019.01.010> (2019).
17. Bergonio, J., Rottas, K. & Schorghofer, N. Properties of martian slope streak populations. *Icarus* <https://doi.org/10.1016/j.icarus.2013.03.023> (2013).
18. Schorghofer, N., Aharonson, O., Gerstell, M. & Tatsumi, L. Three decades of slope streak activity on Mars. *Icarus* <https://doi.org/10.1016/j.icarus.2007.04.026> (2007).
19. Schorghofer, N. & King, C. Sporadic formation of slope streaks on Mars. *Icarus* <https://doi.org/10.1016/j.icarus.2011.08.028> (2011).
20. Marsquake Service Catalog v14 InSight Mars SEIS Data Service 2019 SEIS raw data v14, InSight Mission IPGP, JPL, CNES, ETHZ, ICL, MPS, ISAE-Supaero, LPG, MFSC <https://doi.org/10.12686/a21> (2023).
21. Clinton, J. F. et al. The Marsquake catalogue from InSight, sols 0–478. *Phys. Earth Planet. Inter.* <https://doi.org/10.1016/j.pepi.2020.106595> (2021).
22. Ceylan, S. et al. The marsquake catalogue from InSight, sols 0–1011. *Phys. Earth Planet. Inter.* <https://doi.org/10.1016/j.pepi.2022.106943> (2022).
23. Daubar, I. et al. New craters on Mars: an updated catalog. *JGR Planets* <https://doi.org/10.1029/2021JE007145> (2022).
24. Lucas, A. et al. Possibly seismically triggered avalanches after the S1222a Marsquake and S1000a impact event. *Icarus* <https://doi.org/10.1016/j.icarus.2023.115942> (2024).
25. Forget, F. et al. Improved general circulation models of the Martian atmosphere from the surface to above 80 km. *J. Geophys. Res. Planets* <https://doi.org/10.1029/1999JE001025> (1999).
26. Greeley, R., White, B., Pollack, J., Iversen, J. & Leach, R. Dust storms on Mars: considerations and simulations. *Geol. Soc. Amer. Spec. Paper* **186**, 101–121 (1981).
27. Ayoub, F. et al. Threshold for sand mobility on Mars calibrated from seasonal variations of sand flux. *Nat. Commun.* <https://doi.org/10.1038/ncomms6096> (2014).
28. Newman, C. et al. The dynamic atmospheric and aeolian environment of Jezero crater, Mars. *Sci. Adv.* <https://doi.org/10.1126/sciadv.abn3783> (2022).
29. Newman, C. E., Read, P. L. & Lewis, S. R. Investigating atmospheric predictability on Mars using breeding vectors in a general-circulation model. *Q. J. R. Meteorol. Soc.* **130**, 2971–2989 (2004).
30. Rubanenko, L. et al. Global surface winds and Aeolian sediment pathways on Mars from the morphology of Barchan dunes. *Geophys. Res. Lett.* <https://doi.org/10.1029/2022GL102610> (2023).
31. Gunn, A. & Jerolmack, D. Conditions for aeolian transport in the solar system. *Nat. Astron.* <https://doi.org/10.1038/s41550-022-01669-0> (2022).
32. Swann, C., Sherman, D. J. & Ewing, R. C. Experimentally derived thresholds for windblown sand on Mars. *Geophys. Res. Lett.* <https://doi.org/10.1029/2019GL084484> (2020).
33. Kok, J., Partell, E., Michaels, T. & Bou Karam, D. The physics of wind-blown sand and dust. *Rep. Prog. Phys.* <https://doi.org/10.1088/0034-4885/75/10/106901> (2012).
34. Bickel, V. et al. Dust devil migration patterns reveal strong near-surface winds across Mars. *Sci. Adv.* <https://doi.org/10.1126/sciadv.adw5170> (2025).
35. Rubanenko, L., Perez-Lopez, S., Schull, J. & Lapotre, M. Automatic detection and segmentation of Barchan dunes on Mars and Earth using a convolutional neural network. *IEEE J. Sel. Top. Appl. Earth Obs. Remote Sens.* <https://doi.org/10.1109/JSTARS.2021.3109900> (2021).
36. Vaz, D., Silvestro, S., Chojnacki, M. & Silva, D. Constraining the mechanisms of aeolian bedform formation on Mars through a global morphometric survey. *Earth Planet. Sci. Lett.* <https://doi.org/10.1016/j.epsl.2023.118196> (2023).
37. Baker, M. et al. Coarse sediment transport in the modern Martian environment. *J. Geophys. Res. Planets* <https://doi.org/10.1002/2017JE005513> (2018).
38. Lapotre, M., & Rampe, E. Curiosity's investigation of the Bagnold dunes, Gale Crater: overview of the two-phase scientific campaign and introduction to the special collection. *Geophys. Res. Lett.* <https://doi.org/10.1029/2018GL079032> (2018).
39. Charalambous, C. et al. Vortex-dominated aeolian activity at InSight's landing site, part 1: multi-instrument observations, analysis, and implications. *J. Geophys. Res. Planets* <https://doi.org/10.1029/2020JE006757> (2021).
40. Guzewich, S., Fedorova, A., Kahre, M. & Toigo, A. Studies of the 2018/Mars year 34 planet-encircling dust storm. *J. Geophys. Res. Planets* <https://doi.org/10.1029/2020JE006700> (2020).
41. Giardini, D. et al. The seismicity of Mars. *Nat. Geosci.* <https://doi.org/10.1038/s41561-020-0539-8> (2020).
42. LightShip IDT. LightShip – Instrument Definition Team report v1.0. https://scispace.esa.int/wp-content/uploads/2025/03/LightShip_Instrument_Definition_Team_Final_Report_1.0.pdf (2024).
43. SpotLight MDT. LightShip-1 Passenger S/C “SpotLight” – Measurement Definition Team Report v1.1. https://scispace.esa.int/wp-content/uploads/2025/03/SpotLight_Measurement-Defintion-Team_Final_Report2024_v1.1.pdf (2024).
44. Chuang, F., Beyer, R., McEwen, A. & Thomson, B. HiRISE observations of slope streaks on Mars. *Geophys. Res. Lett.* <https://doi.org/10.1029/2007GL031111> (2007).
45. Sullivan, R., Thomas, P., Veverka, J., Malin, M. & Edgett, K. Mass movement slope streaks imaged by the Mars Orbiter Camera. *J.*

- Geophys. Res. Planets* <https://doi.org/10.1029/2000JE001296> (2001).
46. Lopez-Cayuela, M., Zorzano, M.-P., Guerrero-Rascado, J. & Córdoba-Jabonero, C. Quantitative analysis of the Martian atmospheric dust cycle: transported mass, surface dust lifting and sedimentation rates. *Icarus* <https://doi.org/10.1016/j.icarus.2023.115854> (2024).
 47. Martin, T. Mass of dust in the Martian atmosphere. *J. Geophys. Res. Planets* <https://doi.org/10.1029/95JE00414> (1995).
 48. Bickel, V. T., Loew, S., Aaron, J. & Goedhart, N. A Global perspective on lunar granular flows. *Geophys. Res. Lett.* <https://doi.org/10.1029/2022GL098812> (2022).
 49. Bickel, V. T., Aaron, J., Manconi, A., Loew, S. & Mall, U. Impacts drive lunar rockfalls over billions of years. *Nat. Commun.* **11**, 2862 (2020).
 50. Aussel, B. et al. Global Lunar Boulder Map from LRO NAC optical images using deep learning: implications for regolith and protolith. *J. Geophys. Res. Planets* <https://doi.org/10.1029/2025JE008981> (2025).
 51. Montabone, L. et al. Eight-year climatology of dust optical depth on Mars. *Icarus* <https://doi.org/10.1016/j.icarus.2014.12.034> (2015).
 52. Forget, F. & Montabone, L. Atmospheric dust on Mars: a review. In *47th International Conference on Environmental Systems 2017* <http://hdl.handle.net/2346/72982> (2017).
 53. Guzewich, S., Mason, E., Lemmon, M., Newman, C. & Lewis, K. Dust lifting observations with the Mars Science Laboratory Navigation Cameras. *J. Geophys. Res. Planets* <https://doi.org/10.1029/2023JE007959> (2023).
 54. Balme, M. & Greeley, R. Dust devils on Earth and Mars. *Rev. Geophys.* <https://doi.org/10.1029/2005RG000188> (2006).
 55. Lorenz, R. Heuristic estimation of dust devil vortex parameters and trajectories from single-station meteorological observations: application to InSight at Mars. *Icarus* <https://doi.org/10.1016/j.icarus.2016.02.001> (2016).
 56. Bagnold, R. *The Physics of Blown Sand and Desert Dunes* (Springer Dordrecht, 1941). <https://link.springer.com/book/10.1007/978-94-009-5682-7>.
 57. Sagan, C. & Bagnold, R. Fluid transport on Earth and aeolian transport on Mars. *Icarus* **26**, 209–218 (1975).
 58. Shao, Y., Raupach, M. & Findlater, R. Effect of saltation bombardment on the entrainment of dust by wind. *J. Geophys. Res. Atmos.* <https://doi.org/10.1029/93JD00396> (1993).
 59. Bourke, M., Edgett, K. & Cantor, B. Recent aeolian dune change on Mars. *Geomorphology* <https://doi.org/10.1016/j.geomorph.2007.05.012> (2008).
 60. Kok, J. An improved parameterization of wind-blown sand flux on Mars that includes the effect of hysteresis. *Geophys. Res. Lett.* <https://doi.org/10.1029/2010GL043646> (2010).
 61. Christensen, P. et al. Mars Global Surveyor Thermal Emission Spectrometer experiment: investigation description and surface science results. *J. Geophys. Res. Planets* <https://doi.org/10.1029/2000JE001370> (2001).
 62. USGS. Mars MGS MOLA Global Color Shaded Relief 463m v1. https://astrogeology.usgs.gov/search/map/Mars/GlobalSurveyor/MOLA/Mars_MGS_MOLA_ClrShade_merge_global_463m (2020).
 63. Smith, D. et al. Mars Orbiter Laser Altimeter: experiment summary after the first year of global mapping of Mars. *J. Geophys. Res. Planets* <https://doi.org/10.1029/2000JE001364> (2001).
 64. Stähler, S. et al. Tectonics of Cerberus Fossae unveiled by Mars-quakes. *Nat. Astron.* <https://doi.org/10.1038/s41550-022-01803-y> (2022).
 65. Bickel, V. et al. New impacts on Mars: systematic identification and association with InSight seismic events. *Geophys. Res. Lett.* <https://doi.org/10.1029/2024GL109133> (2025).
 66. Bickel, V. T. Dataset to: Dust, sand and wind drive slope streaks on mars [Dataset]. <https://doi.org/10.48620/91828> (2025).
 67. Thomas, N. et al. The Colour and Stereo Surface Imaging System (CaSSIS) for the ExoMars Trace Gas Orbiter. *Space Sci. Rev.* <https://doi.org/10.1007/s11214-017-0421-1> (2017).

Acknowledgements

The author acknowledges the fellowship funding provided by the Center for Space and Habitability at the University of Bern.

Author contributions

V.T. Bickel: Conceptualization, Methodology, Software, Validation, Formal analysis, Investigation, Resources, Data Curation, Writing - Original Draft, Writing - Review & Editing, Visualization, Project administration, Funding acquisition.

Competing interests

The author declares no competing interests.

Additional information

Supplementary information The online version contains supplementary material available at <https://doi.org/10.1038/s41467-025-65522-4>.

Correspondence and requests for materials should be addressed to Valentin Tertius Bickel.

Peer review information *Nature Communications* thanks the anonymous reviewers for their contribution to the peer review of this work. A peer review file is available.

Reprints and permissions information is available at <http://www.nature.com/reprints>

Publisher's note Springer Nature remains neutral with regard to jurisdictional claims in published maps and institutional affiliations.

Open Access This article is licensed under a Creative Commons Attribution-NonCommercial-NoDerivatives 4.0 International License, which permits any non-commercial use, sharing, distribution and reproduction in any medium or format, as long as you give appropriate credit to the original author(s) and the source, provide a link to the Creative Commons licence, and indicate if you modified the licensed material. You do not have permission under this licence to share adapted material derived from this article or parts of it. The images or other third party material in this article are included in the article's Creative Commons licence, unless indicated otherwise in a credit line to the material. If material is not included in the article's Creative Commons licence and your intended use is not permitted by statutory regulation or exceeds the permitted use, you will need to obtain permission directly from the copyright holder. To view a copy of this licence, visit <http://creativecommons.org/licenses/by-nc-nd/4.0/>.

© The Author(s) 2025